A lower limb non-anthropomorphic wearable robot

Dino Accoto[1,*], Fabrizio Sergi[2], Nevio Luigi Tagliamonte[1], Giorgio Carpino[1], Angelo Sudano[1], Eugenio Guglielmelli[1]

***Abstract*—This paper describes a novel wearable robot intended to assist hip and knee flexion/extension through series elastic actuators. A non-anthropomorphic design was pursued in order to improve ergonomics, while optimizing dynamical properties through a smart distribution of swinging masses. Once the anthropomorphism constraint is relaxed, the number of possible architectures becomes very high, and a methodology must be defined to point out the best options. To this purpose, a design methodology is also presented, which includes a novel approach to kinematic synthesis, topology selection and morphological optimization. The advantages offered by the novel architecture are demonstrated both theoretically and experimentally. In particular, results show a low reflected inertia on the user body, a high backdrivability and an intrinsic tolerance to wearing inaccuracies. Such advantages make the proposed robot a promising platform for the development of assistive and rehabilitation systems.**

I. Introduction

Wearable Robots (WRs) can replace the functions of a missing limb (robotic prostheses) or provide physical assistance to human movements by acting in parallel to the body (active orthoses). Examples of lower-limb portable active orthoses for gait restoration include the Ekso (Ekso Bionics, Berkeley, USA), the ReWalk (Argo Medical Technologies, Yokneam Illit, Israel), the REX (REX Bionics, Auckland, New Zealand), the HAL-5 (Cyberdyne, Tsukuba, Japan), the Vanderbilt Powered Orthosis [1]. Gait assistance can be also provided by treadmill-based robots, which are mainly used in rehabilitation. Examples are the Lokomat (Hocoma, Volketswil, Switzerland), the LOPES (LOwer-extremity Powered ExoSkeleton) [4], the AutoAmbulator (HealthSouth Co., Birmingham, Alabama, USA), the ALEX (Active Leg EXoskeleton) [5], the PAM-POGO (Pelvic Assist Manipulator - Pneumatically Operated Gait Orthosis) [6].

An important objective in the design of an active orthosis is the ergonomics of force transfer. Most of the active orthoses presented so far have anthropomorphic structures with multiple contacts with the human body segments (as opposed to single end-effector robots). This elegant and simple design choice may present some ergonomic drawbacks, as discussed in [7], in terms of *micro-* and *macro-misalignments*. In fact, an anthropomorphic active orthosis can provide selective torque support to a set of human joints if such joints are aligned with the matching DOFs of the robot. Due to inter-subject anthropometric variability, modeling approximations, slippage of robot fixations over the body during motion, a perfect alignment can be hardly achieved. This generates unwanted shear forces on the human skin. To cope with this issue, in [7] special joints are described, capable of decoupling rotations from translations, at the cost of increased inertia and mass: a cost that can be too high in case of portable robots.

Conversely, non-anthropomorphic architectures can be inherently robust against alignment errors. Moreover, the increased design freedom, resulting from the relaxation of the anthropomorphism constraint, offers the appealing opportunity of optimizing the intrinsic dynamics of the robot, e.g. through a proper distribution of masses.

Optimization of robot dynamics is another important target in impedance-controlled active orthoses because at frequencies beyond the controller bandwidth human-robot interaction becomes strongly affected by the intrinsic dynamics of the robot: considering the need of assisting distal joints (i.e. knee and ankle) the mechanical impedance reflected on the user body can become significant.

In this paper we present the design of the LENAR (Lower-Extremity Non-Anthropomorphic Robot), a 4-DOF active orthosis assisting hip and knee flexion/extension during level-ground walking. Using a novel design methodology, the LENAR was conceived and optimized in terms of dynamics (backdrivability) and ergonomics (tolerance to misalignments). The design approach is validated through simulations and experimental tests demonstrating the *intrinsic* backdrivability and the robustness against misalignments.

II. Design

The synthesis of WR structures, which are not anthropomorphic a priori, is a problem with a bewilderingly high number of potential solution. Consequently, the problem of selecting a good solution (possibly the optimal) is not amenable to be tackled using an insight-driven engineering approach, unless the dimensionality of the design space is first adequately reduced. The primitive stage of defining the *topology* of a mechanism, i.e. the number of links and their interconnections, is well-known in mechanical design as *type synthesis*. We addressed this problem for the synthesis of WRs starting from the following assumptions:

- the parallel structure, comprising human segments and robot links, must be able to support and measure independent hip and knee rotations (i.e. 2 DOFs);
- we constrain our search to planar structures confined in the sagittal plane;
- only solutions with revolute joints are considered;

[1]Università Campus Bio-Medico di Roma, Center for Integrated Research (CIR), Laboratory of Biomedical Robotics and Biomicrosystems, Via Álvaro del Portillo, 21 - 00128 Rome, Italy.

[2]Mechatronics and Haptic Interfaces Laboratory, Department of Mechanical Engineering, Rice University, 6100 Main Street, Houston, TX 77005.

[*]Corresponding author: d.accoto@unicampus.it

Preprint submitted to IEEE Robotics and Automation Magazine
Received September 18, 2014 11:53:42 PST

- the robot interacts with the subject through pure forces applied to fixations. Ideal human-robot interaction requires the transfer of forces in the direction orthogonal to body segments.

The developed methodology extends the methods for manipulators type synthesis to include checks on kinematic compatibility of WRs, through the Human-Robot (HR)-degeneracy test [9]. This methodology enabled the exhaustive enumeration of the independent topologies of lower-limb WRs satisfying the above listed assumptions. Such topologies are only ten and are shown in Fig. 1(b).

The ten topologies are equivalent from the mobility standpoint. Therefore, a final choice can be made taking into account ergonomics. We adopted a filtering criterion based on a simple ergonomics principle: a correct interaction requires forces to be applied perpendicularly to human body segments, since tangential forces (shear forces), besides being ineffective for motion generation, may cause discomfort or even tissue damages. It is highly desirable that proper interaction forces are *intrinsically* generated by the robot, thanks to its mechanical structure. If a human segment is connected to the robot through a binary passive link (i.e. a link connected to the rest of the mechanism through two unactuated revolute joints with parallel rotation axes), static forces are perpendicular to both axes, and no torque can be transmitted. If such link remains orthogonal to the human segment it is connected to during robot motion, then the ergonomics goal is achieved. This condition is identified in what follows as the *binary passive link criterion*.

This simple principle, once adopted as a design criterion, provides both a way to select a proper topology, among the ten pointed out so far (Fig. 1(b)), and an objective in the definition of the specific *morphology* (i.e. links length), which must be optimized so that each angle between the connecting passive links and the longitudinal direction of the corresponding human segment (γ and β in Fig. 1(a)) is as close as possible to 90 deg during walking.

Only three topologies (4, 6, and 10) allow to apply the *binary passive link criterion*. Among the three, topology 10 was selected because: *i)* it does not require excessively long links and *ii)* it allows actuators to be placed proximally, i.e. close to the torso, thus reducing the inertia resulting from oscillating masses. Analyzing in more details topology 10, we notice that the satisfaction of the *binary passive link criterion* requires the actuators to be placed in A and D, so that links CF and BE can be passive.

Focusing on topology 10, the set of all the possible values of links length (AH, AD, DE, DF, CF, BE), angle α and positions of fixation points B and C, represents the search space for the optimal morphology. The search was performed by using a scalar fitness function that takes into account some design objectives, in part already introduced in our preliminary work [10].

Using hip and knee angles (θ_h and θ_k) and torques (τ_h and τ_k), obtained from a standard walking dataset [11] (walking speed: 1.4 m/s), we calculated, for every set of morphological parameters, the actuator torques (τ_{m1} and τ_{m2}) and the interaction forces at the fixation points A (torso), B (thigh) and C (shank). Interaction forces at contact points B (shank) and C (thigh) were decoupled into the perpendicular (F_p) and shear (F_s) components. Workspace maximization was introduced as another optimization objective. In particular, robustness of the design with respect to kinematic singularities was quantified and introduced in the fitness function. To this aim, passive joints angles values were individually checked throughout the planar robot workspace. A singularity checking algorithm was implemented to evaluate whether the angle of passive joints fell below a threshold, set to 30 deg. In that case the otherwise null binary variable $sing(\theta_h, \theta_k)$ was set to 1. In the fitness function, the singularity measure was obtained by a 2D summation of $sing(\theta_h, \theta_k)$, weighted by a function ω_i that accounts for the distance between the given posture and the closest point in the nominal Gait Cycle (GC) trajectory.

In order to account for the objectives above, the following scalar objective functions for the torque (f_τ), the force (f_F) and the singularity (f_s) were introduced:

$$\begin{aligned} f_\tau &= \max[\tau_{m_1}(t), \tau_{m_2}(t)]/\tau_{max} \\ f_F &= \max[F_{t,s}(t), F_{s,s}(t)]/F_{max} \\ f_s &= \sum_i \sum_j sing(\theta_{h,i}, \theta_{k,j}) \cdot w_s(\theta_{h,i}, \theta_{k,j}) \end{aligned} \tag{1}$$

having defined the normalization values τ_{max}= 50 N m and F_{max}= 30 N. The scalar fitness function is obtained as the algebraic sum of the normalized objectives in (1). The second objective function (f_F) aims at minimizing shear forces. This corresponds to searching the morphology in which, more than in the others, passive binary links stay orthogonal to the human segments they are connected to.

A hybrid optimization strategy was employed in order to explore the resulting 9-dimensional space. Body segment lengths, retrieved from an anthropometric dataset for a 50% percentile man, were used. The optimization algorithm consisted of the consecutive application of a Genetic Algorithm (GA)[1] and a deterministic Constrained Non-Linear Optimization (CNLO) method[2]. The GA was employed for the preliminary, explorative part of the optimization, while CNLO was used for a local refinement, using as initial guess the best individual produced by the GA. The optimized torque and force profiles are shown in Fig. 2.

The optimized morphology requires a peak actuator torque (52 N m for level-ground walking of a 80 kg mass subject) very close to the peak of hip and knee torques, calculated via inverse kinematics (48 N m). Furthermore, the maximum shear force transferred to the supported body segments is 29 N, i.e. only 13% of the peak perpendicular forces. The singularity-free workspace corresponds to the set $\theta_h \in (-20, 45)$ deg, $\theta_k \in (0, 65)$ deg and fully contains hip and knee angles obtained during normal walking. For other daily life activities

[1]Implemented through the optimization toolbox of Matlab R2011b, the Mathworks. GA parameters: Population Size: 40, Max Generations: 100, Scattered Crossover with Fraction 0.8, Elite count: 2, Migration Fraction: 0.4, Migration Interval: 5, Stall Generations Limit: 15, Function Tolerance: 10^5.

[2]The "active-set" algorithm was used. Maximum number of iterations: 100, Parameters Termination Tolerance: 10^9.

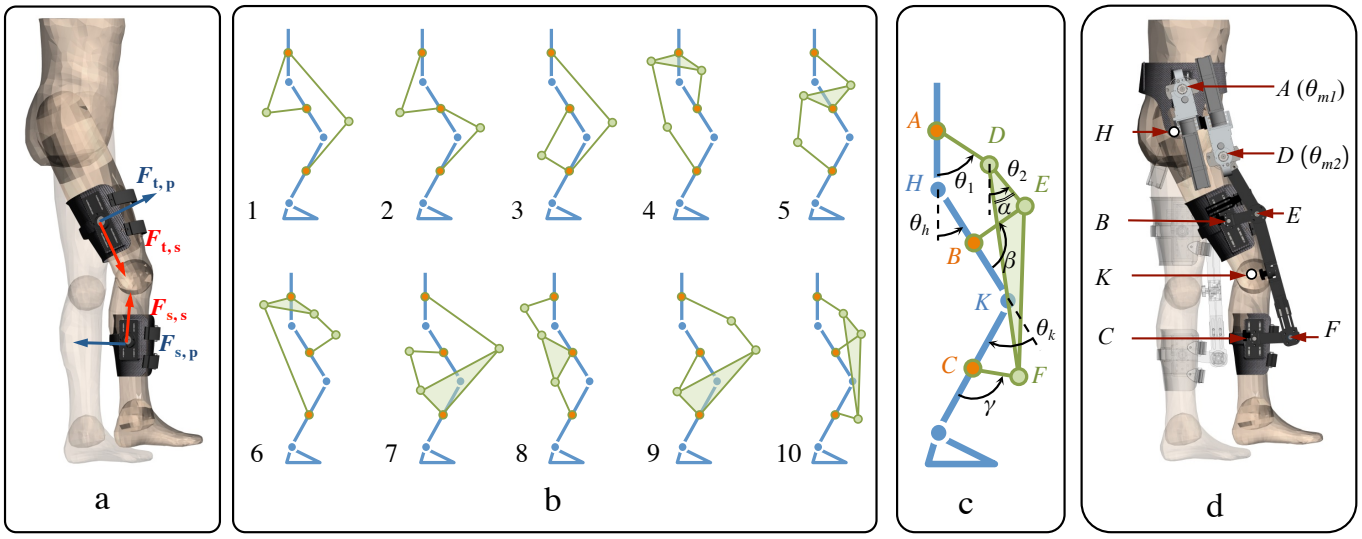

Fig. 1. The different stages of the pursued design process, from problem definition (left), to mechanisms enumeration (center), to design optimization and detailed mechanical design (right). (a) Interaction forces between human segments and wearable robots. For gait assistance in the sagittal plane, desired forces F_p are perpendicular to the addressed limbs axes, while shear forces F_s are undesired. (b) Arbitrary morphological representation of the ten generalized solutions for the design problem. Human segments and articulations are reported in blue. Robot joints are reported in orange (on attachment sites) and in green. (c) Kinematic scheme of the mechanism used for morphology optimization, that includes both human segments (blue lines) and robot links (green lines). (d) 3D CAD design. Blank circles, points H and K, represent the human hip and knee joints respectively. Points A and D are the actuated robotic joints, also indicated as m_1 and m_2. Actuator rotations are ($\theta_{m_1} = \theta_1$ and $\theta_{m_2} = \theta_2 - \theta_1$). Points B, C, E and F are robot passive revolute joints.

(e.g. ascending/descending stairs, squatting) a different optimization process would be required. Nonetheless the range of motion allowed by the robot corresponds to 100% of the mean physiological values [12] for hip extension, to 38% of hip flexion and 45% of knee flexion.

A schematic of the resulting mechanism is shown in Fig. 1(d). The optimized solution was fabricated and integrated with custom designed actuators, as detailed in Sec. III-A.

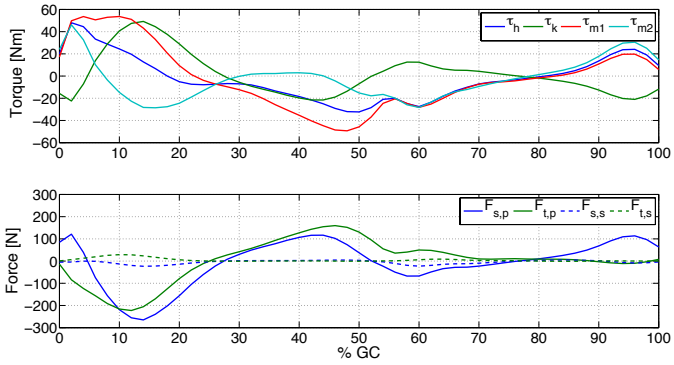

Fig. 2. Profiles of actuator torques and of forces at the attachment points B (thigh, $F_{t,p}$ and $F_{t,s}$) and C (shank, $F_{s,p}$ and $F_{s,s}$), for the optimized solution. The values refer to the level-ground walking of a subject with mass of 80 kg, walking speed: 1.4 m/s.

III. Prototype Development

A. Actuators and control

Custom rotary Series Elastic Actuators (SEAs) were purposively designed. The actuators include a hypoid gear transmission that enables shifting the actuator center of mass with respect to the actuated joint, resulting in the gearmotor being placed alongside human limbs [13]. Through the compliant element, the gearmotor reflected inertia can be decoupled from the load and can be used to implement an accurate torque control using the elastic element as a torque sensor. Moreover, passive series elasticity allows impacts tolerance and rejection of disturbances due to cyclic foot strike events, reduction of stiction, friction and backlash and energy buffering. In each SEA (picture in Fig. 3(a)), a Maxon EC-4pole brushless DC motor (rated power: 300 W) is connected to the output shaft through a monolithic disc-shaped torsion spring (Fig. 3(b)). Spring design was based on an iterative FEM simulation-based design and optimization process [14]. A double reduction stage (comprised of a planetary gear box and a hypoid gear – overall reduction ratio: 64.5:1, efficiency: 76.5%) is placed between the motor and the elastic element. Spring deflection is measured using two Gurley A10 absolute encoders (resolution: $1.9{\cdot}10^{-4}$ rad). The actuators provide a maximum continuous torque of 30 N m and a peak torque of 60 N m.

SEAs are torque-controlled through the measurement of the spring deflection. The control scheme is based on the cascaded approach proposed in [15]. It consists of a PI velocity control loop nested in a PI torque control loop. The robot is stiffness-controlled in its joint space[3], i.e. the desired torque for each actuated joint (right leg r and left leg l) is set as:

$$\tau_{m_i,d}(t) = -k_{m_i}[\theta_{m_i}(t) - \theta_{m_i,d}(t)] \qquad (2)$$

being θ_{m_i} and $\theta_{m_i,d}$ the actual and the desired actuator rotations respectively, and k_{m_i} the virtual stiffness ($i = 1, 2$).

[3]The space defined by actuator rotations $(\theta_{m_1}, \theta_{m_2})$.

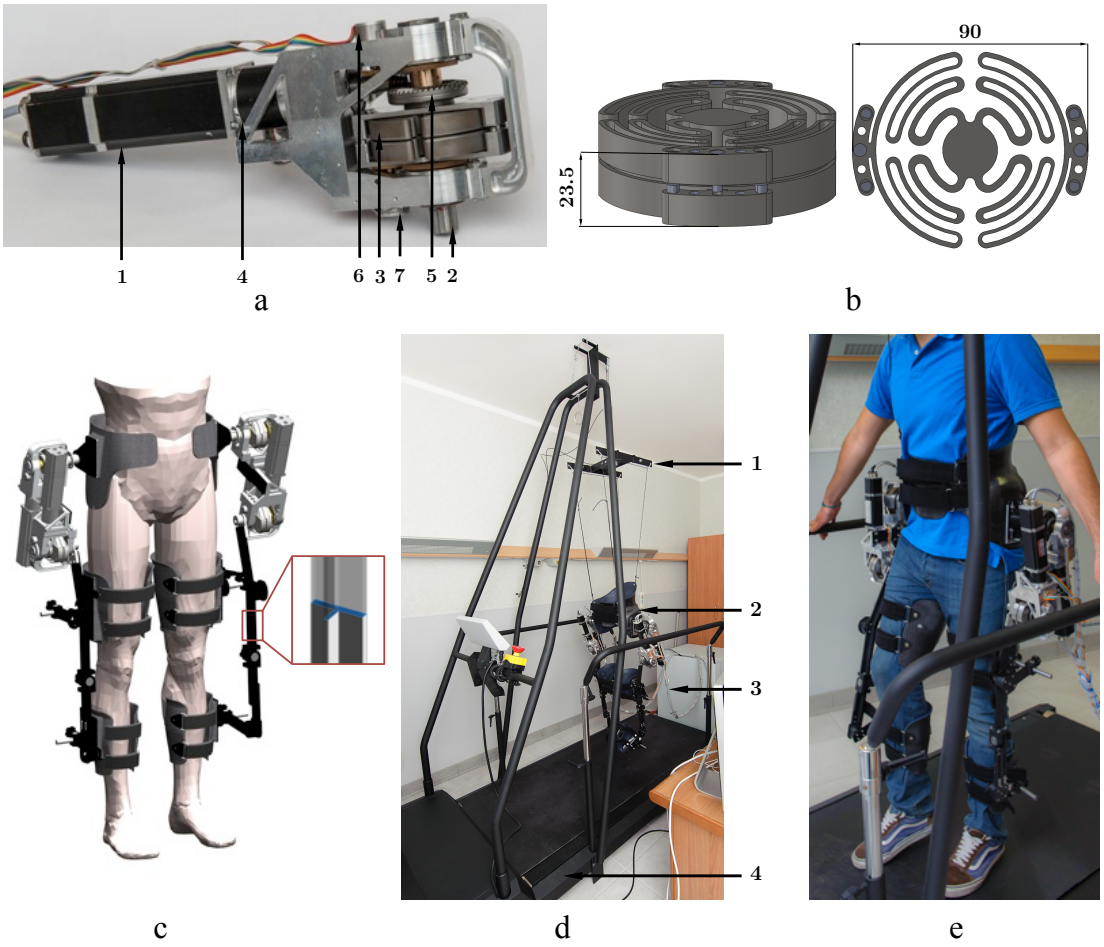

Fig. 3. (a) Rotary SEA. 1: DC motor; 2: Output shaft; 3: Torsion spring; 4: Planetary gear box; 5: Hypoid gear; 6-7: Absolute encoders. (b) 3D CAD drawing of the torsion spring. (c) 3D CAD drawing of the LENAR with a detail of the links T-shaped cross section. (d) Treadmill-based platform. 1: Robot weight support system; 2: Wearable robot; 3: Electronic rack; 4: Treadmill. (e) The LENAR worn by a subject.

The control hardware consists of: *i)* Four Maxon EPOS2 70/10 control units to drive SEA brushless DC motors, connected to two Maxon Shunt Regulators DSR 70/30 limiting supply voltage increases. *ii)* A National Instruments compactRIO-9022 unit (cRIO), with a reconfigurable Field-Programmable Gate Array (FPGA) module and an embedded controller running LabVIEW Real Time (RT) software. The cRIO also comprises two high-speed digital I/O modules (NI 9403) as interfaces with robot encoders, and a high-speed (1 Mbit/s) CAN module (NI 9853) for communication with the EPOS2 units. The FPGA module acquires SEA absolute encoder signals (SSI communication, 10 kHz), runs torque controllers (1 kHz) and executes CAN bus low-level communication with the EPOS2 units (transmission of motor commands and reading of current, position and velocity). Torque controllers generate desired velocity set-points that are transmitted via CANopen protocol to the velocity controllers running on the EPOS2 devices (1 kHz). The high-level stiffness controller runs on the cRIO RT level at 200 Hz. Feedback for torque and stiffness controllers are based on the measurement of the absolute encoders, filtered using second-order lowpass Butterworth filters, with a cut-off frequency of 40 Hz. All the control components and power supplies are located in a remote rack.

Experimental characterization confirmed the predicted torsional stiffness of the spring ($k_s = 270.2$ N m/rad). The torque control bandwidth of the actuator in blocked output conditions is 6.5 Hz [13]. Stiffness control performance was evaluated with the actuator commanded to generate elastic torques with different values of the virtual stiffness k_m, while keeping $\theta_{m,d}$ fixed. In these conditions the output shaft was manually perturbed with oscillatory movements (amplitude of about 80 deg). Tests were carried out varying k_m in the range $[0.1\,k_s,\ k_s]$, with steps of $0.1\,k_s$. The estimated mechanical impedance transfer function $\hat{Z}(f)$, calculated by using a non-parametric identification method [13], is reported in Fig. 4. Data are shown in the range 0.6 – 6 Hz, where the coherence between the imposed velocity and the interaction torque was found to be greater than 0.8 for all the tests. The performance degradation in rendering a virtual stiffness much lower than the physical one (k_s) is in line with literature results [19].

As expected from theoretical studies [20] the system becomes not passive (phase of $\hat{Z}(f)$ smaller than -90 deg) for $k_m > 0.6\,k_s$. Anyhow, since passivity is a conservative condi-

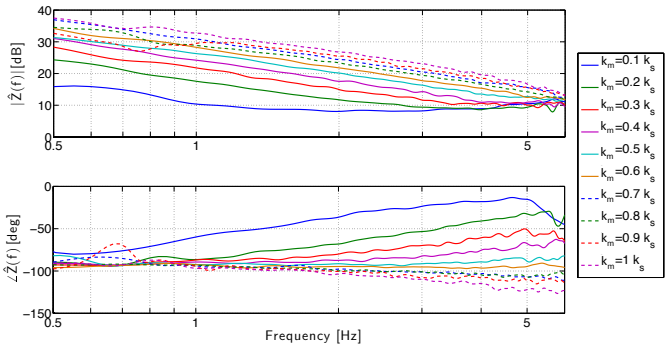

Fig. 4. Bode diagram of the SEA transfer function $\hat{Z}(f)$ when rendering a pure elastic behavior with different virtual stiffness values k_m. For $k_m > 0.6\,k_s$ the system becomes not passive (dashed lines) as expected from theoretical studies [20].

TABLE I
PROTOTYPE PERFORMANCE.

Quantity	Measure	Unit
SEAs		
Maximum continuous torque	30	N m
Peak torque	60	N m
Maximum continuous speed	5.8	rad/s
Rated power	300	W
Intrinsic stiffness	270.2	N m/rad
Torque control bandwidth (30 N m ptp)	6.5	Hz
Robot		
Hip maximum back-driving torques	10	N m
Knee maximum back-driving torques	5	N m
Hip range of motion	45 (flex) – 20 (ext)	deg
Knee range of motion	65 (flex) – 0 (ext)	deg
Maximum walking speed	5	km/h
User height	1.65 – 1.85	m

tion for coupled stability, no stability issues were experienced during interaction tests with manual perturbations.

To estimate the order of magnitude of torques needed by the robot to move itself (i.e. in free space, compensating gravitational and frictional effects), physiological walking movements were produced with the robot suspended to the frame and with the actuators stiffness-controlled. With reference to Fig. 1(c), starting from hip and knee desired rotations $\theta_{h,d}$ and $\theta_{k,d}$, it was possible to derive, based on inverse kinematics calculations, actuator rotations $\theta_{m_{1,d}}$ and $\theta_{m_{2,d}}$ to be used in the stiffness control (2) and needed to produce the desired kinematic patterns in the human joint space. Data on hip and knee physiological patterns ($\theta_{h,d}$ and $\theta_{k,d}$) in the sagittal plane for healthy young subjects were retrieved from [11]. These data were adapted to a slow-walking GC duration (3.2 s) and angles amplitude was scaled by a factor 1.4. The same profile was used for both legs, with a phase shift of π. Virtual stiffness was set to $k_{m_{il}} = k_{m_{ir}} = 0.2\,k_s$ for $i = 1, 2$. Results, shown in Fig. 5 demonstrated that the system can produce the desired walking patterns with peak actuation torques lower than 7 N m, i.e. 12% of the maximum value allowed by the actuators. Therefore, 88% of the actuator deliverable torques is still available to provide physical assistance during walking and to compensate for dynamical effects. A summary of the limit performance of the developed prototype is reported in Tab. I.

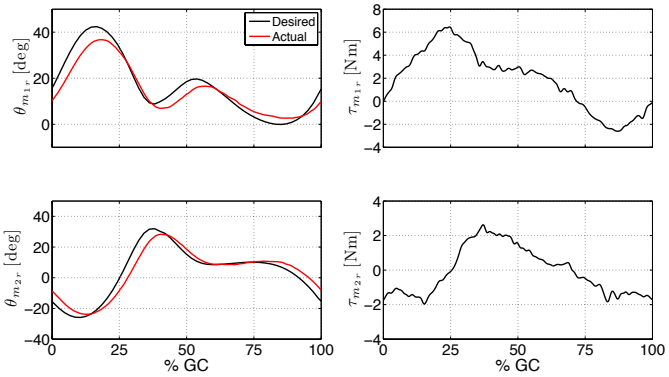

Fig. 5. Tests when moving the robot (right leg) in the free space. Desired positions for the stiffness controller were offline calculated from the inverse kinematics problem to achieve physiological gait in the human joints space (data adapted from [11]).

B. Wearing and usage

With reference to Fig. 1(d), the LENAR comprises a pelvis cuff (hosting joint A) and, for each leg, two SEAs actuating joints A and D, one thigh cuff (hosting joint B) and one shank cuff (hosting joint C). The segment EF can be adjusted to accommodate users between the 5$^{\text{th}}$ and the 95$^{\text{th}}$ percentile of adult population (see Table I). Sliders allow the regulation of the position of joints A, B and C. To reduce the parasitic compliance due to links flexion-torsion the links were built from class 7075 aluminum alloy (Ergal), using a T-shape cross section. Moreover, the carbon fiber cuffs embed an aluminum insert for increased stiffness. An overview of the WR is shown in Fig. 3(c).

As shown in Fig. 3(d), the robot is suspended over a treadmill (N-Mill, ForceLink B.V; walking surface of 70×175 cm^2) through a passive vacuum cylinder, which provides an upward constant force equal to the weight of the robot (about 25 kg), without introducing serial elasticity and possible resonances. The height of the support can be manually adjusted to accomodate users with different anthropometric measures. Cables are used to connect the weight support system to the pelvis cuff. This allows passive pelvis rotations. Hip adduction/abduction motion is also allowed by the compliance of the carbon fiber pelvis cuff. Intra/extra rotation, which is not necessary for walking on a treadmill, is constrained.

When the user accesses the platform, the pelvis cuff is adjusted in a comfortable position. Then the suspension height is regulated by manually acting on the weight balancing system. Subsequently, Velcro straps on the pelvis cuff are fastened. Then, the thigh and shank cuffs are worn and fastened. Adjustable links and sliders on the cuffs (see section III-B) are regulated to allow links BE and CF (see Fig. 1(d)) to be almost perpendicular to the human segments.

IV. Advantages of non-anthropomorphism

A. Dynamic analysis

A dynamic analysis based on the Generalized Inertia Ellipsoid (GIE) [18] in the human joint space (θ_h, θ_k) during normal walking [11] helps assessing the potential benefits introduced by the non-anthropomorphic design. The dynamics of a n DOFs robotic system can be written as:

$$M(q)\ddot{q} + C(q,\dot{q})\dot{q} + g(q) = \tau, \tag{3}$$

where q is the $n\times 1$ vector of generalized coordinates, $M(q)$ is the $n\times n$ inertia matrix, $C(q,\dot{q})$ is the $n\times n$ matrix representing Coriolis/centrifugal terms, $g(q)$ is the $n\times 1$ gravity vector, and τ is the $n \times 1$ vector of actuation forces/torques applied on the generalized coordinates.

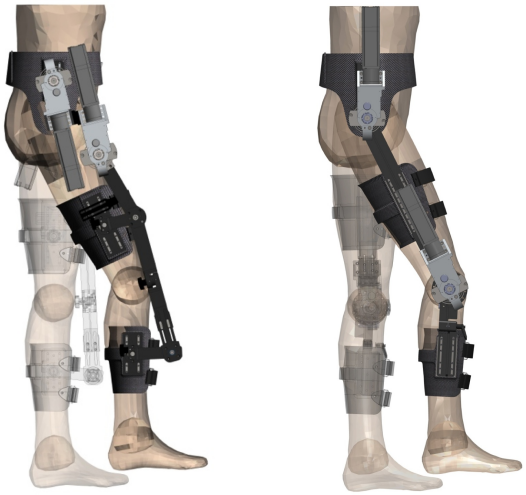

Fig. 6. Schematic of the two models considered for the dynamic analysis of the robot. (N-A) Non-anthropomorphic robot (LENAR). (A) Anthropomorphic robot using the same actuators of the LENAR.

We compared the equivalent inertia reflected at the hip and knee joints by the *non-anthropomorphic robot* (N-A), with the one calculated in two conditions: *a)* the *no-robot condition* (N-R), in which only the intrinsic inertia of the legs is reflected on the hip and knee joints; *b)* the *anthropomorphic robot condition* (A), in which the same actuators described in Sec. III-A are used in an anthropomorphic architecture. To simplify the comparison, in both A and N-A cases the actuators are assumed to be directly connected to the corresponding actuated joints, although actuators remotization could improve the dynamic performance of both architectures. In this analysis, we consider the torso grounded and we focus on the swing since it is the phase mostly dominated by inertia.

To make the comparison conservative (i.e. slightly biased in favor of the A architecture), we introduced further assumptions on the A structure: *i)* the stator of the hip actuator is framed to the torso, so that only its rotor contributes to the inertia reflected at the hip and gravitational effects are minimized; *ii)* knee actuator is placed so that its center of mass is as proximal as possible (to minimize the associated swinging mass); *iii)* links are massless.

The impedance perceived by a user can be quantified by the inertia matrix alone, since full inverse dynamics simulations, taking into account both human segments and robotic links, evidenced that the peak and RMS values of the torques calculated for the $C(q,\dot{q})$ matrix, are much lower than inertial torques for the N-A, N-R and A conditions. For instance, the peak Coriolis contribution is 7% of the peak inertial torque for the hip joint and 20% for the knee joint.

The mass needed to support a distal joint (in our case the knee joint) obviously increases the inertial load on the proximal joint (in our case the hip joint) (Fig. 7). However, the N-A design reduces such increase compared to the A case. The inertia (λ_1) perceived when moving in the principal direction is calculated as the square root of the maximum eigenvalue of the quadratic form $M^T(q)M(q)$.

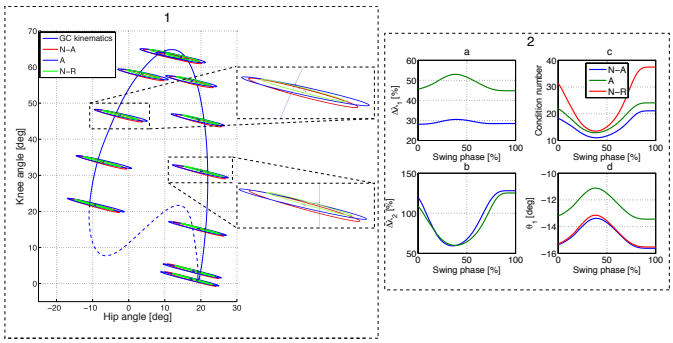

Fig. 7. (1) Comparison of the resulting inertia for the non-anthropomorphic design described in this paper (N-A), the equivalent anthropomorphic system (A), and the no-robot condition (N-R), as determined by the equivalent inertia ellipses in the human joint space during the swing phase (continuous line in the GC depicted). A standard gait pattern moves clockwise along the blue line. (2) Ratio between the maximum (a) and minimum (b) eigenvalue of the inertia matrix for the N-A and A systems and the correspondent eigenvalue of the N-R condition, in the same posture. (c) Condition number throughout the stance phase. (d) Measure of rotation of the principal axis of inertia, relative to the N-R case, for both the N-A condition and the A condition, throughout the swing phase.

To quantify the effect of the robot design on the resulting inertia, we considered the measures depicted in Fig. 7. The first two measures are the percent increase of λ_i, for both the N-A and A robots, compared to the value of λ_i calculated for each posture in the N-R condition:

$$\Delta\lambda_i^j(t) = 100\frac{\lambda_i^j(q(t))}{\lambda_i^{N-R}(q(t))}, \qquad i = 1,2. \tag{4}$$

The subscript i refers to either the maximum (for $i = 1$) or to the minimum (for $i = 2$) eigenvalue of the inertia matrix quadratic form, whereas the subscript j refers to the N-A condition, and to the A condition. Further, we define the condition number ($\kappa(M)$) of the inertia matrix as a measure of inertial anisotropy in each considered posture of the swing phase. The condition number is the ratio between the maximum and minimum inertia matrix eigenvalues. Finally, we quantify the rotation of the principal axis (θ_1^j), by measuring the angle between the principal vector v_1^j ($j = N\text{-}R, A$) and the $\hat{\theta}_h$ unit vector as $\theta_1^j = \text{acos}(v_i^j \cdot \hat{\theta}_h)$.

A higher value of θ_1^j results in a larger angle between the principal axis of inertia v_1 and the hip angle coordinate axis $\hat{\theta}_h$, which implies a reduction of the equivalent inertia displayed at the hip joint (keeping the shape of the ellipse constant).

We summarized in Table II the mean and standard deviation (STD) of the four measures of interest during the swing phase, as well as the absolute values corresponding to the N-R condition. The analysis of the average resulting inertia of the non-anthropomorphic robot shows a 29% increase of the maximum principal value, compared to the N-R condition, while the lowest principal value increases by 93%. The unavoidable increase of perceived inertia, due to the need of oscillating masses to support the distal joint, is lower than the increase in inertia in the A design. In particular, the increase of the lowest principal value is substantially the same in the N-A and A cases, while the increase in the principal eigenvalue is higher in the A case (48% vs. 29%). The parameter chosen to represent the orientation of the inertia ellipse θ_1^j is related to the relative contribution of inertia perceived at the hip joint compared to the inertia perceived at the knee joint; its analysis shows that the N-A design minimally perturbs the orientation of the inertia ellipse, compared to the N-R condition. Instead, the A design results in an ellipse with a more horizontal principal axis, reflecting the disproportionate relative increase in the inertia perceived at the hip joint compared to the one reflected to the knee joint.

The condition number in the N-A is 15.4, compared to 18.1 of the A solution, indicating that the inertia perceived by the user is more isotropic in the two axes. Although the N-R solution has an even higher degree of anisotropy of the displayed inertia (23.8), this is due to the fact that the minimum eigenvalue λ_2 is only equal to 0.12 kg m^2, and the necessity of supporting the distal joints unavoidably increases this value, hence increasing the condition number.

TABLE II
DYNAMICAL COMPARISON OF THE NON-ANTHROPOMORPHIC ROBOT (λ_i ARE IN KG M^2 AND θ_1 IS IN DEG).

	N-A	A	N-R
λ_1 - Mean	3.33	3.83	2.5
λ_1 - STD	0.26	0.25	0.21
$\Delta\lambda_1$ - Mean	29	48	–
$\Delta\lambda_1$ - STD	0.8	3	–
λ_2 - Mean	0.22	0.21	0.12
λ_2 - STD	0.03	0.03	0.03
$\Delta\lambda_2$ - Mean	92.4	88.1	–
$\Delta\lambda_2$ - STD	25.76	23.6	–
$\kappa(M)$ - Mean	15.4	18.1	23.8
$\kappa(M)$ - STD	3.6	4	8.7
θ_1 - Mean	-14.6	-12.4	-14.5
θ_1 - STD	0.8	0.8	0.8

B. Backdrivability

Backdrivability was assessed through experimental tests aimed at evaluating muscular activity and torques needed to backdrive the robot while walking at different speeds (1.8, 2.7 and 3.6 km/h). Before the tests, the subject (male, 24 y.o., height 178 cm, body mass 90 kg) was asked to walk freely at a self-selected cadence for 10 minutes to get familiar with the device and with the testing environment. A picture of the subject wearing the robot is reported in Fig. 3(e). Tri-axis accelerometers (DE-ACCM3D, Dimension Engineering), whose signals were acquired through a NI 9205 analog input module, were placed on the heels of the subject shoes in order to detect the foot contact with the ground. The subject was first asked to walk at different walking speeds without the robot (No Robot, N-R), in order to set the baseline, and then wearing the robot with actuators switched off (Unpowered Robot, U-R). Surface EMG electrodes (DENIS 5026, Spes Medica), connected to two 4-channel amplifiers (QP522, Grass Technologies), were used to measure muscular activity. The activity of five muscles on the right leg was measured: rectus femoris, vastus lateralis, tibialis anterior, gastrocnemius medialis, biceps femoris. Signals were band-pass filtered ($10 - 1000$ Hz) and acquired with the cRIO control unit through the NI 9205 module (sampling frequency: 2 kHz). During post processing, signals were full-wave rectified and low-pass filtered by using a zero-lag second order Butterworth filter with cut-off frequency 5 Hz for smoothing. Data were segmented based on heel contact events, averaged over 30 s of trial and normalized with respect to the peak value of the EMG activity (for each muscle and for each walking speed) of the N-R tests.

During the tests, joint rotations ($\theta_{m_{ir}}$ and $\theta_{m_{il}}$, $i = 1, 2$) and human-robot interaction torques ($\tau_{m_{ir}}$ and $\tau_{m_{il}}$, $i = 1, 2$) in the robot joint space were recorded. Angles (θ_h, θ_k) and torques (τ_h, τ_k) of the hip and knee joints were calculated using the transformation from the robot joint space to the human joint space. Actuator and human joint angles, averaged over 30 s in steady-state condition, are reported in Fig. 9, for the test at the different walking speeds. The mean GC duration for the tests in N-R mode was 1.7 s, 1.4 s and 1.2 s respectively. In the human joint space, peak backdriving torques were 6.2 N m, 10.0 N m and 12.6 N m for the three selected speeds (knee joint). With unpowered actuators, a subject has to deliver low additional torques to backdrive the robot (around in the range 11–23% of those required during free overground walking). This result quantitatively demonstrates the intrinsic backdrivability of the robot, enabled by the reduced inertia reflected on the body and by the low impedance of the actuators.

The reduced perturbation to the human natural motion was also demonstrated by the EMG signals reported in Fig. 8, where muscular activities in the U-R and N-R conditions are compared. It can be noticed that the presence of the robot, although unpowered, produces major alterations to natural muscular activation only at low walking speeds. In particular, with respect to the N-R condition, at 1.8 km/h the RMS activity of the RF and of the VL are about doubled, the one of the TA and GM decreases by about 40% and the one of the BF increases by about 30%. Moreover, the maximum EMG variation occurs, at all the walking speeds, for the RF and the VL.

Finally, walking cadence in U-R condition changed less than 30% at the three different speeds (recorded GC durations: 1.8 s, 1.4 s and 1.3 s respectively).

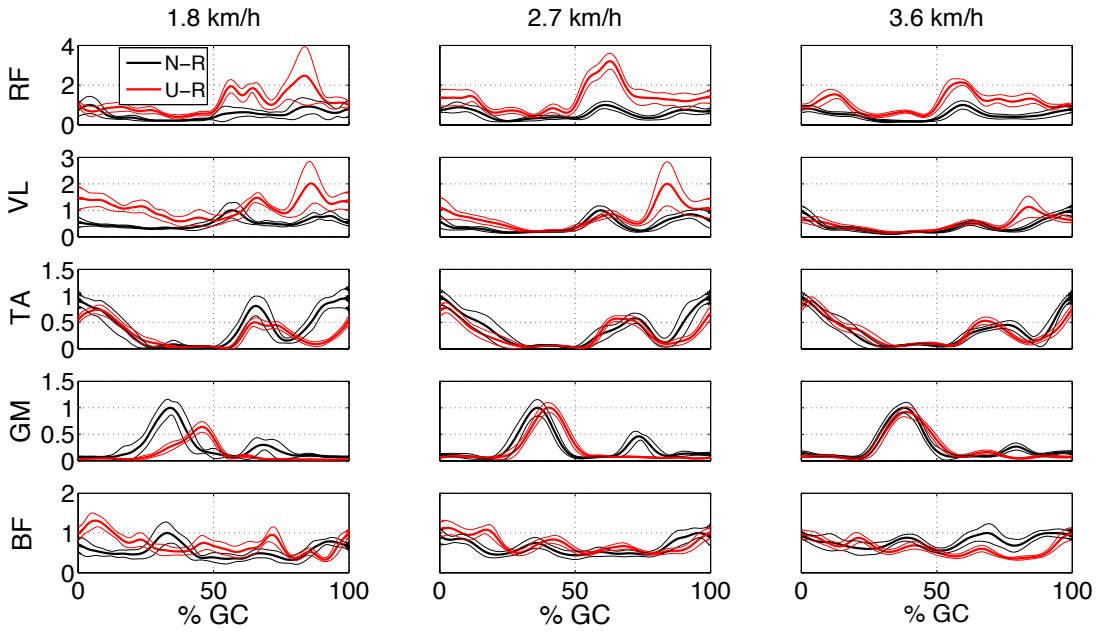

Fig. 8. EMG activity of rectus femoris (RF), vastus lateralis (VL), tibialis anterior (TA), gastrocnemius medialis (GM), biceps femoris (BF) for the tests at three different speeds with the subject during free walking (N-R) and wearing the unpowered robot (U-R). Thin lines indicate standard deviation.

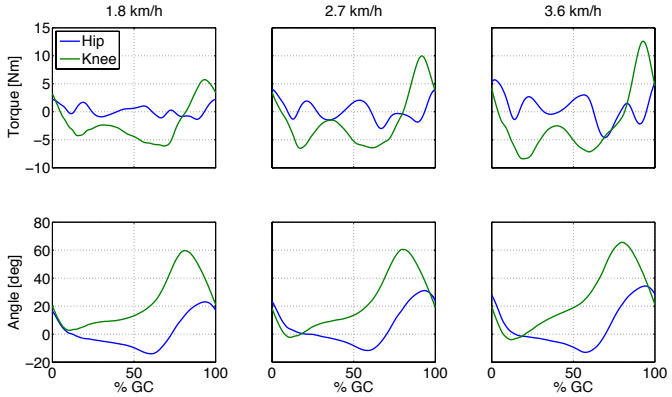

Fig. 9. Human-robot interaction torques in the human joint space (as a function of the percentage of the GC) and joint rotations for the backdrivability tests performed at different walking speeds. Data are averaged over 30 s for each trial.

TABLE III
CALIBRATION PARAMETERS.

Link/segment	BK	DF	KC	EF
Robot aligned				
Length [mm]	150	560	240	370
Robot misaligned				
Length [mm]	140	530	210	340

C. Tolerance to misalignments

Tolerance to misalignments simplifies both wearing and calibration procedures. To demonstrate such tolerance, which is the second objective pursued with the design methodology, numerical analysis and experimental tests were performed.

The sensitivity of shear forces during walking to the non-optimal placement of the fixation points was investigated numerically. We moved points A, B and C ($\pm$5 mm with steps of 2.5 mm) to simulate 125 misalignment conditions. In the worst case, peak shear forces were about 30% and 18% of the peak perpendicular forces (compared to 13% of the ideal case), for the thigh and the shank attachment points respectively.

We also complemented the analysis with experimental trials repeating the tests described in Sec. IV-B with the robot calibrated to fit a user about 5 cm shorter than the real tester (Tab. III). The user, who was asked to self-select the walking speed (2.7 km/h), showed a GC duration which did not significantly differ from the case the robot was correctly mounted. As shown in Fig. 10, kinematic patterns, human joint delivered torques and EMG activity were not significantly altered when the robot was misaligned.

In detail, the RMS variation of the hip torque (τ_h) is 1.1 N m, while the RMS variation of the knee torque (τ_k) is 2.0 N m. The RMS variation of hip and knee angles are 2.1 deg and 5.2 deg, respectively. The variation of EMG signals is not statistically significant. Last but not least, no perceivable discomfort was reported.

V. Discussion and Conclusions

Because of their simplicity, anthropomorphic architectures are by far the most used in assistive and rehabilitation robotics. Such architectures, mounted in parallel to the human body, require that robot and human joints are accurately aligned, as misalignments would result in kinematic incompatibilities impeding the movement of the limbs or causing physical discomfort. Moreover, fixing the topology of the robot reduces the degrees of freedom the designer can exploit to endow the robot with desired dynamical features, such as the minimization of

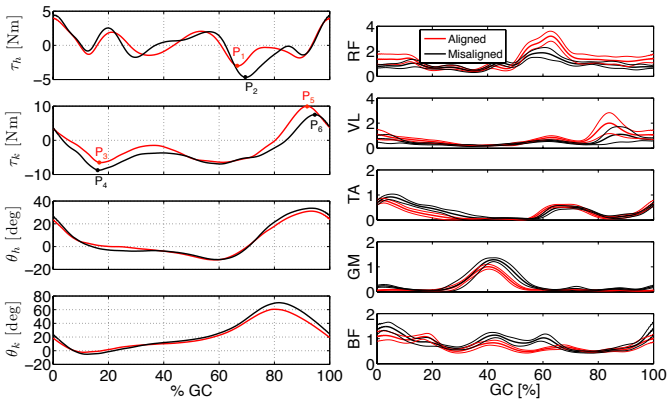

Fig. 10. Comparison between torques, angles and EMG activity during tests with the robot optimally mounted on the subject and with the introduction of mounting errors at a self-selected walking speed of 2.7 km/h. Thin lines indicate standard deviation. Maximum peak torque increases at hip and knee joints respectively are 56% (between P_1 and P_2) and 34% (between P_3 and P_4). Peak torque at knee decreases by 25% between points P_5 and P_6.

swinging masses and the intrinsic control of the direction of the interaction forces.

The LENAR was designed starting from the relaxation of the anthropomorphism constraint. This tremendously enlarges the search space for type synthesis. In this paper we presented a design approach based on *a)* the systematic search of all robot configurations with a desired mobility to provide mechanical support to a given number of human joints, *b)* the selection of a candidate design solution and *c)* the design optimization to improve ergonomics and actuation requirements. Through the novel methodology pursued, it was possible to improve, compared to an equivalent anthropomorphic design, both the dynamical properties, in terms of reflected inertia, and the ergonomics of force transfer, in terms of robustness to wearing misalignments. Such aspects were validated both numerically and experimentally, as summarized below.

As for dynamic improvements, the analysis of the average resulting inertia of the non-anthropomorphic robot shows a 29% increase for the maximum principal value, compared to the no-robot condition. Such increase is smaller than the one that would occur in an anthropomorphic design using the same actuators (48%). The increase in the lowest principal value of inertia is high in both robot designs (93% for the N-A and 89% for the A), but applies to a direction characterized by a significantly smaller inertial loading (in average, 0.21 kg m^2 compared to 3.3 km m^2 for the proximal joint). To further investigate the dynamical properties, we defined a parameter that indicates the orientation of the displayed inertia ellipse, in human joint space. This parameter describes the relative contribution of inertia perceived at the hip joint compared to the inertia perceived at the knee joint. Our analysis shows that the non-anthropomorphic design minimally perturbs the orientation of the inertia ellipse, compared to the no-robot condition. Instead, the anthropomorphic design results in a ellipse with a principal axis much more aligned with the hip joint axis, reflecting the disproportionate relative increase in the inertia perceived at the hip joint compared to the one reflected to the knee joint. The analysis also demonstrates that the proposed design mitigates the unavoidable increase in equivalent inertia displayed to the human joints. Based on the assumptions of the comparison, it can be concluded that the dynamical advantages are intrinsic to the morphology of the designed N-A robot. Indeed, any real anthropomorphic robot, i.e. with links with not null mass, using the same actuation system, would exhibit a dynamic performance lower than that of the LENAR. Such result supports the choice of a non-anthropomorphic design in lower-limb active orthoses, given the fact that walking is a dynamical process dominated by inertia.

Another important feature of the proposed design is that it locates the actuators, which are the heaviest swinging masses, close to the torso. Despite the high torque and power of the actuators used (2 compliant actuators per leg, each with a peak torque of 60 N m and a rated power of 300 W), the robot is highly backdrivable even when unpowered, with backdriving torques in the human joint space corresponding to 11–23% of those delivered by human joints during free overground walking. This results was also confirmed by small alterations in EMG activity of five muscles of a single leg when compared to the case the subject walked without wearing the robot.

As for ergonomics, the possibility to allow fast wearing procedures is an often overlooked feature of WRs, especially in the rehabilitation scenario, where it is of prominent importance the maximization of the time devoted to the actual therapy. Under this regard, the non-anthropomorphic structure simplifies the wearing procedure, since the robot joints must not be aligned to human joints. We could estimate that the first wearing procedure with a new subject takes about 15–25 minutes, while about 5–10 minutes are enough for successive procedures. Interaction tests, performed with robot link lengths set at different values from the reference ones, demonstrated no significant alterations to the EMG activity and to torque and angle profiles.

The proposed design approach lends itself to the future development of both novel treadmill-based rehabilitation robots (e.g. with remotized actuators) and novel robots with full mobility (e.g. with portable controllers and energy source).

References

[1] R. Farris, H. Quintero, and M. Goldfarb, "Preliminary evaluation of a powered lower limb orthosis to aid walking in paraplegic individuals," *Neural Systems and Rehabilitation Engineering, IEEE Transactions on*, 2011.

[2] P. D. Neuhaus, J. H. Noorden, T. J. Craig, T. Torres, J. Kirschbaum, and J. E. Pratt, "Design and evaluation of mina: A robotic orthosis for paraplegics," in *Rehabilitation Robotics (ICORR), 2011 IEEE International Conference on*, pp. 1 – 8, 2011.

[3] T. Nakamura, K. Saito, Z. Wang, and K. Kosuge, "Realizing a posture-based wearable antigravity muscles support system for lower extremities," in *Rehabilitation Robotics, 2005. ICORR 2005. 9th International Conference on*, pp. 273 – 276, 2005.

[4] J. Veneman, R. Kruidhof, E. Hekman, R. Ekkelenkamp, E. V. Asseldonk, and H. van der Kooij, "Design and evaluation of the lopes exoskeleton robot for interactive gait rehabilitation," *Neural Systems and Rehabilitation Engineering, IEEE Transactions on*, vol. 15, no. 3, pp. 379 – 386, 2007.

[5] S. Banala, S. H. Kim, S. Agrawal, and J. Scholz, "Robot Assisted Gait Training With Active Leg Exoskeleton (ALEX)," *Neural Systems and Rehabilitation Engineering, IEEE Transactions on*, vol. 17, no. 1, pp. 2 – 8, 2009.

[6] D. Aoyagi, W. Ichinose, S. Harkema, D. Reinkensmeyer, and J. Bobrow, "A robot and control algorithm that can synchronously assist in naturalistic motion during body-weight-supported gait training following neurologic injury," *Neural Systems and Rehabilitation Engineering, IEEE Transactions on*, vol. 15, pp. 387 –400, 2007.
[7] A. Stienen, E. Hekman, F. van der Helm, and H. van der Kooij, "Self-aligning exoskeleton axes through decoupling of joint rotations and translations," *Robotics, IEEE Transactions on*, vol. 25, no. 3, pp. 628 – 633, 2009.
[8] X. Kong and C. Gosselin, *Type synthesis of parallel mechanisms*, vol. 33. Springer, 2007.
[9] F. Sergi, D. Accoto, N. L. Tagliamonte, G. Carpino, and E. Guglielmelli, "A systematic graph-based method for the kinematic synthesis of non-anthropomorphic wearable robots for the lower limbs," *Frontiers of Mechanical Engineering*, vol. 6, pp. 61–70, 2011.
[10] F. Sergi, D. Accoto, N. L. Tagliamonte, G. Carpino, and E. Guglielmelli, "Kinematic synthesis, optimization and analysis of a non-anthropomorphic 2-DOFs wearable orthosis for gait assistance," in *IEEE/RSJ International Conference on Intelligent Robots and Systems (IROS 2012)*, 2012.
[11] D. Winter, *Biomechanics and Motor Control of Human Movement*. Wiley, 2009.
[12] A. Roaas and G. B. J. Andersson, "Normal range of motion of the hip, knee and ankle joints in male subjects, 30-40 years of age,", *Acta Orthopaedica*, vol. 53, pp. 205–208, 1982.
[13] D. Accoto, G. Carpino, F. Sergi, N. L. Tagliamonte, L. Zollo, and E. Guglielmelli, "Design and characterization of a novel high-power series elastic actuator for a lower limb robotic orthosis," *Int J Adv Robot Syst*, vol. 10, 2013.
[14] G. Carpino, D. Accoto, F. Sergi, N. L. Tagliamonte, and E. Guglielmelli, "A novel compact torsional spring for series elastic actuators for assistive wearable robots," *Journal of Mechanical Design*, vol. 134, no. 12, pp. 121002:1 – 10, 2012.
[15] H. Vallery, J. Veneman, E. van Asseldonk, R. Ekkelenkamp, M. Buss, and H. van der Kooij, "Compliant actuation of rehabilitation robots: benefits and limitations of series elastic actuators," *IEEE Robotics & Automation Magazine*, vol. 15, no. 3, pp. 60 – 69, 2008.
[16] L. W. Tsai, *Robot Analysis and Design: The Mechanics of Serial and Parallel Manipulators*. New York, NY, USA: John Wiley & Sons, Inc., 1st ed., 1999.
[17] F. H. Ghorbel, O. Chételat, R. Gunawardana, and R. Longchamp, "Modeling and set point control of closed-chain mechanisms: theory and experiment," *Control Systems Technology, IEEE Transactions on*, vol. 8, no. 5, pp. 801 – 815, 2000.
[18] H. Asada, "A geometrical representation of manipulator dynamics and its application to arm design," *Journal of Dynamic Systems, Measurement, and Control*, vol. 105, no. 3, pp. 131 – 142, 1983.
[19] F. Sergi, D. Accoto, G. Carpino, N. Tagliamonte, and E. Guglielmelli, "Design and characterization of a compact rotary series elastic actuator for knee assistance during overground walking," in *Biomedical Robotics and Biomechatronics (BioRob), IEEE RAS EMBS International Conference on*, pp. 1931 –1936, 2012.
[20] N. L. Tagliamonte and D. Accoto, "Passivity constraints for the impedance control of series elastic actuators," *Proceedings of the Institution of Mechanical Engineers, Part I: Journal of Systems and Control Engineering*, vol. 228, no. 3, pp. 138 – 153, 2014.